SUPPORTING INFORMATION

Phase-resolved surface plasmon scattering probed by cathodoluminescence holography

Nick J. Schilder, * Harshal Agrawal, Erik C. Garnett, and Albert Polman

Center for Nanophotonics, AMOLF

Science Park 104, 1098 XG Amsterdam, The Netherlands

1. Optical constants of the stack

Figure S1 shows the dispersion for both Ag (Fig. S1a) and SiO_x (Fig. S1b) retrieved from spectroscopic ellipsometry.

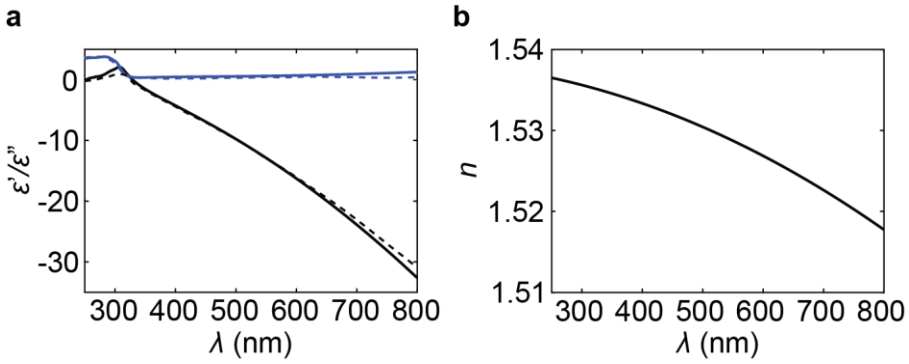

Figure S1. Optical constants derived from spectroscopic ellipsometry data. (a) Dielectric constant of evaporated Ag (solid curves) and from Johnson and Christy (dashed curves). The real/imaginary part of the dielectric constants are shown in black/blue. (b) Refractive index of evaporated SiO_x.

2. Angle-dependent visibility for surface plasmon scattering from nanocube

Since the angular scattering intensities for transition radiation and surface plasmon scattering are not the same, the interference fringe visibility is angle-dependent. The visibility of a sinusoidal signal is defined as the amplitude divided by the mean: $V = \frac{(I_{\max} - I_{\min})/2}{(I_{\max}+I_{\min})/2}$. In Section S4, we find $I_{\mathrm{tot}}(\theta,\phi) = I_{\mathrm{ref,p}} + I_{\mathrm{sc,p}} + I_{\mathrm{sc,s}} + \frac{\varepsilon_0 c}{2} E_{\mathrm{ref,p}} E^*_{\mathrm{sc,p}} + \frac{\varepsilon_0 c}{2} E^*_{\mathrm{ref,p}} E_{\mathrm{sc,p}}$. We generalize the visibility to a system with a non-uniform envelope. The angle-dependent maximum intensity $I_{\max}(\theta,\phi) = I_{\mathrm{ref,p}} + I_{\mathrm{sc,p}} + I_{\mathrm{sc,s}} + 2\sqrt{I_{\mathrm{ref,p}} I_{\mathrm{sc,p}}}$ and the minimum intensity $I_{\min}(\theta,\phi) = I_{\mathrm{ref,p}} + I_{\mathrm{sc,p}} + I_{\mathrm{sc,s}} - 2\sqrt{I_{\mathrm{ref,p}} I_{\mathrm{sc,p}}}$. From the retrieved scattered intensities of SPPs and TR (Fig. 5) we calculated the angle-dependent fringe visibility *V* for the nanocube

$$V(\theta,\phi) = \frac{2\sqrt{I_{\mathrm{TR}} I_{\mathrm{sc,p}}}}{I_{\mathrm{TR}} + I_{\mathrm{sc,p}} + I_{\mathrm{sc,s}}}. \quad \text{(S1)}$$

over the entire azimuthal and zenithal angle range (Fig. S2). We find that for the angular range along the k_x axis, where the CL intensity is highest (k_x/k_0=-0.7--0.6) and the data most accurate, *V*=0.15.

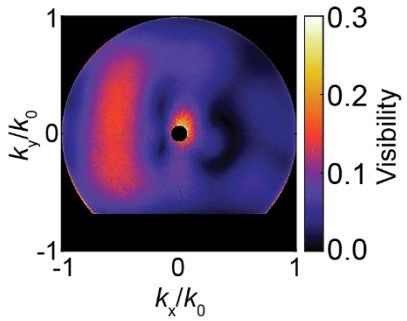

Figure S2. Angle-dependent fringe visibility derived from Fourier analysis data in Fig. 5.

In experiments the visibility of the interference fringes is affected by the 40 nm bandwidth of the color filter. The left/right asymmetry of the visibility can partially be ascribed to the finite temporal coherence of the fields, which we derive now.

Since cathodoluminescence is spectrally broadband, the measured angular radiation pattern after passing through a color filter is given by :

$$I_{\text{interference}}(\theta,\phi) = \frac{\varepsilon_0 c}{2}\frac{1}{\Delta\lambda}\int_{\lambda_c-\frac{\Delta\lambda}{2}}^{\lambda_c-\frac{\Delta\lambda}{2}} E_{\text{TR}}(\theta,\phi,\lambda)\cdot E^*_{\text{sc,p}}(\theta,\phi,\lambda)\mathrm{d}\lambda. \text{ (S2)}$$

Transition radiation and the scattered field are synchronized with the impact of the incident electron. The optical path difference between the scattered field and transition radiation is given by $k_0 n_{\text{eff}}(\lambda)L_e + k_0 L_e \sin\theta$, where $k_0 n_{\text{eff}}(\lambda)$ is the propagation constant of the surface plasmon, which follows from the dispersion relation. Filling in this (dispersive) optical path difference into Eq. S2 leads to:

$$I_{\text{interference}}(\theta,\phi) = \frac{\varepsilon_0 c}{2}\frac{1}{\Delta\lambda}\int_{\lambda_c-\frac{\Delta\lambda}{2}}^{\lambda_c-\frac{\Delta\lambda}{2}} E_{\text{TR}}(\theta,\phi,\lambda)\cdot {E^*_{\text{sc,p}}}^{(0)}(\theta,\phi,\lambda)e^{-ik_0 L_e[n_{\text{eff}}(\lambda)+\sin\theta]}\mathrm{d}\lambda. \text{ (S3)}$$

We assume transition radiation, the scattered fields, and the surface plasmons to be dispersionless over the 40 nm bandwidth of the used color filter. We also perform a change of variables $\lambda = \lambda_c + \lambda'$, where λ_c is the central wavelength of the color filter. The deviation from the central wavelength λ' is small given the narrow bandwidth, hence one can approximate $k_0 = \frac{2\pi}{\lambda} \approx \frac{2\pi}{\lambda_c}\left(1-\frac{\lambda'}{\lambda_c}\right)$. Equation S3 then becomes:

$$I_{\text{interference}}(\theta,\phi) = \frac{\varepsilon_0 c}{2}E_{\text{TR}}(\theta,\phi)\cdot {E^*_{\text{sc,p}}}^{(0)}(\theta,\phi)\frac{1}{\Delta\lambda}\int_{-\frac{\Delta\lambda}{2}}^{-\frac{\Delta\lambda}{2}} e^{-i\frac{2\pi}{\lambda_c}\left(1-\frac{\lambda'}{\lambda_c}\right)L_e[n_{\text{eff}}(\lambda_c)+\sin\theta]}\mathrm{d}\lambda'. \text{ (S4)}$$

This integration leaves us with

$$|I_{\text{interference}}(\theta,\phi)| = \frac{\varepsilon_0 c}{2}|E_{\text{TR}}(\theta,\phi)|\cdot|{E^*_{\text{sc,p}}}^{(0)}(\theta,\phi)||\text{sinc}\left\{\frac{\Delta\lambda}{2\lambda_c}k_0 L_e[n_{\text{eff}}(\lambda_c)+\sin\theta]\right\}|, \text{ (S5)}$$

where $k_0 = \frac{2\pi}{\lambda_c}$. Filling in Eq. S5 into Eq. S1, one finds:

$$V = \frac{2\sqrt{I_{\text{TR}}I_{\text{sc,p}}|\text{sinc}\left\{\frac{\Delta\lambda}{2\lambda_c}k_0 L_e[n_{\text{eff}}(\lambda_c)+\sin\theta]\right\}|}}{I_{\text{TR}}+I_{\text{sc,p}}}, \text{ (S6)}$$

Since the sinc-function has an upperbound of 1, we indeed observe that the visibility is in general reduced for any finite bandwidth of the colorfilter.

3. Definition of Fourier transform

The convention of the Fourier transform is in this work is:

$$f(x,y) = \iint f\left(k_{\text{x}},k_{\text{y}}\right)e^{i(k_{\text{x}}x+k_{\text{y}}y)}\frac{\mathrm{d}k_{\text{x}}\mathrm{d}k_{\text{y}}}{(2\pi)^2}, \quad \text{(S7a)}$$

$$f\left(k_{\text{x}},k_{\text{y}}\right) = \iint f(x,y)e^{-i(k_{\text{x}}x+k_{\text{y}}y)}\mathrm{d}x\mathrm{d}y. \quad \text{(S7b)}$$

4. Numerical algorithm to retrieve both amplitude and phase of the scattered field

The numerical algorithm applied to retrieve both amplitude and phase of the scattered field is similar to the theoretical framework in Ref. [2]. The far-field electric field consists of the p-polarized electric field of transition radiation ($E_{\mathrm{ref,p}}$) and the scattered electric field from the nanoscatterer that in general can have both an s- and p-polarized component ($E_{\mathrm{sc,s}}$ and $E_{\mathrm{sc,p}}$). The far-field radiation pattern $I_{\mathrm{tot}}(\theta,\phi) \propto \left|E_{\mathrm{tot,p}}(\theta,\phi)\hat{\boldsymbol{p}}(\theta,\phi) + E_{\mathrm{tot,s}}(\theta,\phi)\hat{\boldsymbol{s}}(\theta,\phi)\right|^2$. Because of the orthogonality of p- and s-polarized electric fields, one finds for the far-field radiation pattern $I_{\mathrm{tot}}(\theta,\phi) \propto \left[\left|E_{\mathrm{tot,p}}(\theta,\phi)\right|^2 + \left|E_{\mathrm{tot,s}}(\theta,\phi)\right|^2\right]$. For notational brevity we remove the angular dependences of the electric fields. The total electric field is composed of the reference field E_{ref} and the scattered field E_{sc}: $I_{\mathrm{tot}} \propto \left[\left|E_{\mathrm{ref,p}}\right|^2 + \left|E_{\mathrm{sc,p}}\right|^2 + E^*_{\mathrm{ref,p}} \cdot E_{\mathrm{sc,p}} + E_{\mathrm{ref,p}} \cdot E^*_{\mathrm{sc,p}} + \left|E_{\mathrm{ref,s}}\right|^2 + \left|E_{\mathrm{sc,s}}\right|^2 + E^*_{\mathrm{ref,s}} \cdot E_{\mathrm{sc,s}} + E_{\mathrm{ref,s}} \cdot {E^*_{\mathrm{sc,s}}}^2\right]$. The reference field in this work is transition radiation, which is fully p-polarized for symmetry reasons, so $E_{\mathrm{ref,s}} = 0$. Since the proportionality factor for the norm of the Poynting vector I_{tot} is $\frac{\varepsilon_0 c}{2}$, one finds for the far-field radiation pattern:

$$I_{\mathrm{tot}} = I_{\mathrm{ref,p}} + I_{\mathrm{sc,p}} + I_{\mathrm{sc,s}} + \frac{\varepsilon_0 c}{2} E_{\mathrm{ref,p}} E^*_{\mathrm{sc,p}} + \frac{\varepsilon_0 c}{2} E^*_{\mathrm{ref,p}} E_{\mathrm{sc,p}}. \quad \text{(S8)}$$

The radiation pattern is composed of the radiation of the reference field ($I_{\mathrm{ref,p}}$), the total radiation from the scatterer ($I_{\mathrm{sc,p}}$+$I_{\mathrm{sc,s}}$) and two terms that represent interference between the reference field and the scattered field ($E_{\mathrm{ref,p}}E^*_{\mathrm{sc,p}}$ and $E^*_{\mathrm{ref,p}}E_{\mathrm{sc,p}}$). We replace the angles θ and ϕ by the normalized wave vector components: $k_x/k_0=\sin(\theta)\cos(\phi)$ and $k_y/k_0=\sin(\theta)\sin(\phi)$ ($k_0=2\pi/\lambda_c$, with λ_c is the central wavelength of the band-pass filter). The in-plane position vector of the nanoscatterer $\boldsymbol{r}_{\mathrm{sc}}=\langle x, y\rangle$ is defined in a reference frame with the excitation point of the electron beam at the origin. Within the far-field approximation, the scattered electric field is given by

$$E_{\mathrm{sc,p/s}} = E^{(0)}_{\mathrm{sc,p/s}} e^{-i\langle k_x, k_y\rangle \cdot \boldsymbol{r}_{\mathrm{sc}}}, \quad \text{(S9)}$$

with the superscript 0 indicating that the corresponding field has as origin $\boldsymbol{r}_{\mathrm{sc}}$. Taking the 2D Fourier transform of the far-field intensity pattern results in

$$\tilde{I}_{\mathrm{tot}}(\boldsymbol{r}) = \tilde{I}_{\mathrm{ref,p}}(\boldsymbol{r}) + \tilde{I}_{\mathrm{sc,p}}(\boldsymbol{r}) + \tilde{I}_{\mathrm{sc,s}}(\boldsymbol{r}) + \frac{\varepsilon_0 c}{2}\tilde{E}_{\mathrm{ref,p}}(\boldsymbol{r}+\boldsymbol{r}_{\mathrm{sc}}) * \tilde{E}^{(0)*}_{\mathrm{sc,p}}(\boldsymbol{r}+\boldsymbol{r}_{\mathrm{sc}}) + \frac{\varepsilon_0 c}{2}\tilde{E}^*_{\mathrm{ref,p}}(\boldsymbol{r}-\boldsymbol{r}_{\mathrm{sc}}) * \tilde{E}^{(0)}_{\mathrm{sc,p}}(\boldsymbol{r}-\boldsymbol{r}_{\mathrm{sc}}). \quad \text{(S10)}$$

Both the scattered field and transition radiation originate from a subwavelength region, hence the spatial extent of all electric fields $\tilde{E}$ is roughly λ (diffraction limit). The convolution of two functions that have both a spatial extent of λ results in a function with a typical length scale $\sqrt{2}\lambda$. This means that the interference terms, previously described, are spatially separated from the individual intensities terms $[\tilde{I}_{\mathrm{ref,p}}(\boldsymbol{r}) + \tilde{I}_{\mathrm{sc,p}}(\boldsymbol{r}) + \tilde{I}_{\mathrm{sc,s}}(\boldsymbol{r})]$ when the nanoscatterer is placed at least $\sqrt{2}\lambda$ away from the electron beam, as is the case in this work. We apply a mask to $\tilde{I}_{\mathrm{tot}}(\boldsymbol{r})$, such that only the term of interest $\tilde{E}_{\mathrm{ref,p}}(\boldsymbol{r}+\boldsymbol{r}_{\mathrm{sc}}) * \tilde{E}^{(0)*}_{\mathrm{sc,p}}(\boldsymbol{r}+\boldsymbol{r}_{\mathrm{sc}})$ is non-zero. Note that the mask could also be applied to the term $\tilde{E}^*_{\mathrm{ref,p}}(\boldsymbol{r}-\boldsymbol{r}_{\mathrm{sc}}) * \tilde{E}^{(0)}_{\mathrm{sc,p}}(\boldsymbol{r}-\boldsymbol{r}_{\mathrm{sc}})$ instead. This mask is chosen to be $\mathrm{rect}\left(\frac{|\boldsymbol{r}-\boldsymbol{r}_{\mathrm{sc}}|}{L}\right)$, where L=2 μm, and multiplied by Eq. S5. Subsequently, we shift the data by +$\boldsymbol{r}_{\mathrm{sc}}$, so that the masked interference terms is placed in the origin, resulting in

$$\tilde{I}_{\mathrm{tot,masked\&shifted}}(\boldsymbol{r}) = \frac{\varepsilon_0 c}{2}\tilde{E}_{\mathrm{ref,p}}(\boldsymbol{r}) * \tilde{E}^{(0)*}_{\mathrm{sc,p}}(\boldsymbol{r})\mathrm{rect}\left(\frac{|\boldsymbol{r}|}{L}\right). \qquad \text{(S11)}$$

Performing the 2D inverse Fourier transform then results in an approximation of

$$I_{\mathrm{tot,masked\&shifted}}\left(\frac{k_x}{k_0},\frac{k_y}{k_0}\right) = \frac{\varepsilon_0 c}{2}E_{\mathrm{ref,p}}\left(\frac{k_x}{k_0},\frac{k_y}{k_0}\right)\cdot E^{(0)*}_{\mathrm{sc,p}}\left(\frac{k_x}{k_0},\frac{k_y}{k_0}\right). \qquad \text{(S12)}$$

Finally, by using $E_{\mathrm{ref,p}}\left(\frac{k_x}{k_0},\frac{k_y}{k_0}\right) = \sqrt{\frac{2}{\varepsilon_0 c}I_{\mathrm{ref,p}}\left(\frac{k_x}{k_0},\frac{k_y}{k_0}\right)}$, the complex p-polarized scattered field can be obtained by:

$$E^{(0)}_{\mathrm{sc,p}}\left(\frac{k_x}{k_0},\frac{k_y}{k_0}\right) = \left(\frac{I_{\mathrm{tot,masked\&shifted}}\left(\frac{k_x}{k_0},\frac{k_y}{k_0}\right)}{\sqrt{\frac{\varepsilon_0 c}{2}I_{\mathrm{ref,p}}\left(\frac{k_x}{k_0},\frac{k_y}{k_0}\right)}}\right)^{*}. \qquad \text{(S13)}$$

With this, we arrive at the final equation that is used to retrieve the complex-valued p-polarized scattered field as a function of the normalized wave vector components.

5. Far-field phase profile for transition radiation

Here, we show that the wave front for transition radiation in the SiO_x/Ag/Si stack is close to spherical and therefore uniform in our representation in (k_x/k_0, k_y/k_0) space. We calculate the far-field phase profile numerically by approximating the source by a z-polarized electric dipole 10 nm above the stack. Figure S3a shows from which angle $k_\parallel/k_0=\sin(\theta)$, the deviation of the phase is more than $\pi/10$ as compared to the phase for $k_\parallel/k_0=0.001$. From Fig. S3a we find that the phase profile of our reference field can be considered uniform when $k_\parallel/k_0<0.9$.

Next, we show in Fig. S3b the phase of transition radiation at $k_\parallel/k_0=0.7$ for λ=375-820 nm. The wavelength-dependent phase originates from the material dispersion of the stack. The phase difference within the wavelength range λ=580-620 nm is approximately $\pi/50$, which is negligible for the experimental results shown in Figs. 2, 5, and S2.

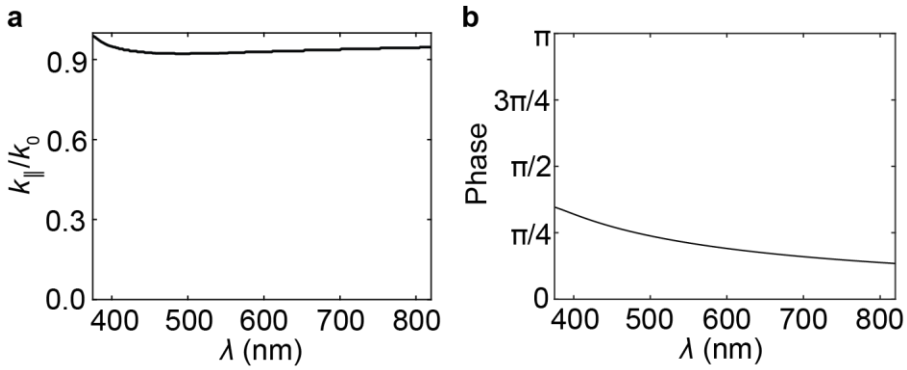

Figure S3. Far-field phase profile for transition radiation. (a) Lower threshold value of $k_\parallel/k_0$ for which the transition radiation phase deviates more than $\pi/10$ from the phase at $k_\parallel/k_0=0.001$. (b) Far-field phase of transition radiation for λ=375-820 nm at $k_\parallel/k_0=0.7$.

6. Multipole expansion

In homogeneous space, the electric fields on a sphere can be decomposed in the orthonormal basis of vector spherical harmonics. Each basis function can be identified with one multipole radiating at the origin of the sphere.

In this manuscript, we retrieve the (complex) p-polarized electric field in part of the upper hemisphere, defined by the parabolic mirror collecting CL. The retrieved p-polarized electric field in the upper hemisphere is decomposed in the non-orthogonal basis spanned by the p-polarized electric fields produced by multipoles placed at 10 nm above the stack. We limit ourselves to electric and magnetic dipoles. The p-polarized emission collected by the parabolic mirror forms 56%, 52% and 100% of the total emission that is collected for x-, y-, and z-polarized electric dipoles, respectively. For x-, y-, and z-polarized magnetic dipoles, this is 56%, 61%, and 0%, respectively. As we only retrieve the p-polarized electric field, and a z-polarized magnetic dipole uniquely emits s-polarized electric fields, we are insensitive to the z-polarized magnetic dipole. Hence, any emission originating from a z-polarized magnetic dipole cannot be retrieved with this experimental technique. We therefore omit this dipole in the analysis. All fields, including the retrieved electric fields, are normalized as follows:

$$\iint_{\mathrm{NA}} \left|E_{\mathrm{MP,p}}(\mathrm{k_x}, k_\mathrm{y})\right|^2 \mathrm{d}k_\mathrm{x}\mathrm{d}k_\mathrm{y} = 1, \quad \text{(S14)}$$

where the NA is determined by the parabolic mirror. The amplitude and phase of the complex expansion coefficients are obtained as follows:

$$c_{\mathrm{MP}} = \iint_{\mathrm{NA}} E_{\mathrm{sc,p}}(\mathrm{k_x}, k_\mathrm{y}) E^*_{\mathrm{MP,p}}(\mathrm{k_x}, k_\mathrm{y}) \mathrm{d}k_\mathrm{x}\mathrm{d}k_\mathrm{y}. \qquad \text{(S15)}$$

The coefficients for the nanohole and the nanocubes are listed in Table S1 and S2, respectively. A graphical representation of the results presented in Table S1 and S2 is presented in Fig. 3 of the main text. We found that the contribution of the different scattering components is somewhat sensitive to the precise shape of the hole: comparing measurements on different holes with slightly varying dimensions we find variations in amplitude of typically 10-20%, and with some exceptional larger deviations.

Table S1. *Coefficients of multipole expansion for SPP scattering from nanohole.*

	p_x	p_y	p_z	m_x	m_y
Amplitude	0.80	0.13	0.46	0.14	0.78
Phase (π)	0.00	1.22	1.82	0.74	0.50

The electron beam was placed L_e=2.29 μm to the right.

Table S2. *Coefficients of multipole expansion for SPP scattering from Ag nanocube.*

	p_x	p_y	p_z	m_x	m_y
Amplitude	0.40	0.30	0.72	0.32	0.41
Phase (π)	0.00	0.55	1.42	0.05	0.51

The electron beam was placed L_e=2.29 μm to the right.

Next, we check the orthogonality of the electric fields emitted by different dipoles(MP_i, and MP_j), by calculating

$$c_{\mathrm{MPij}} = \iint_{\mathrm{NA}} E_{\mathrm{MPi,p}}(\mathrm{k_x}, k_\mathrm{y}) E^*_{\mathrm{MPj,p}}(\mathrm{k_x}, k_\mathrm{y}) \mathrm{d}k_\mathrm{x} \mathrm{d}k_\mathrm{y}. \qquad \text{(S16)}$$

The amplitude of c_{MPij} is presented in Table S3. We observe that the electric fields emitted by different dipoles are not orthogonal. The non-zero value obtained for p_z and p_y can be explained by the limited collection angles along the y axis due to the parabolic mirror. As a consequence, we have observed in Fig. 3b of the main text that a strong z-polarized electric dipole comes together with a y-polarized electric dipole, even though this dipole cannot be excited due to symmetry arguments of the sample and excitation process. Even though the basis is not orthogonal and Eq. S15 is therefore strictly not valid, interesting trends can be learned from this analysis (see main text). For completeness, we provide an orthogonal basis for the in-plane dipoles that follows from a Gram-Schmidt process: p_x+im_y, p_y+im_x, (p_x-im_y)-0.1i(p_x+im_y), (p_y-im_x)+0.1i(p_y+im_x).

Table S3. *Orthogonality of far-fields from all combinations of dipoles.*

	$\boldsymbol{p_x}$	$\boldsymbol{p_y}$	$\boldsymbol{p_z}$	$\boldsymbol{m_x}$	$\boldsymbol{m_y}$
$\boldsymbol{p_x}$	1.00	0.00	0.00	0.00	1.00
$\boldsymbol{p_y}$	0.00	1.00	0.14	1.00	0.00
$\boldsymbol{p_z}$	0.00	0.14	1.00	0.16	0.00
$\boldsymbol{m_x}$	0.00	1.00	0.16	1.00	0.00
$\boldsymbol{m_y}$	1.00	0.00	0.00	0.00	1.00

Absolute value of overlap integral of far-field electric fields for all combinations of dipoles according to Eq. S15.

7. Surface plasmon polariton scattering from nanocubes

Figures S4a-c show the total (a) and reference (b) intensity from which data in Fig. 5 was derived, and the 2D fast Fourier transform of the difference (c). Figures S4d-f show the total intensity (d) for a NC where the electron beam was placed L_e=3.85 μm to the right of the NC, (e) the 2D fast Fourier transform of I_{tot} - I_{ref} and (f) shows the retrieved far-field scattering pattern.

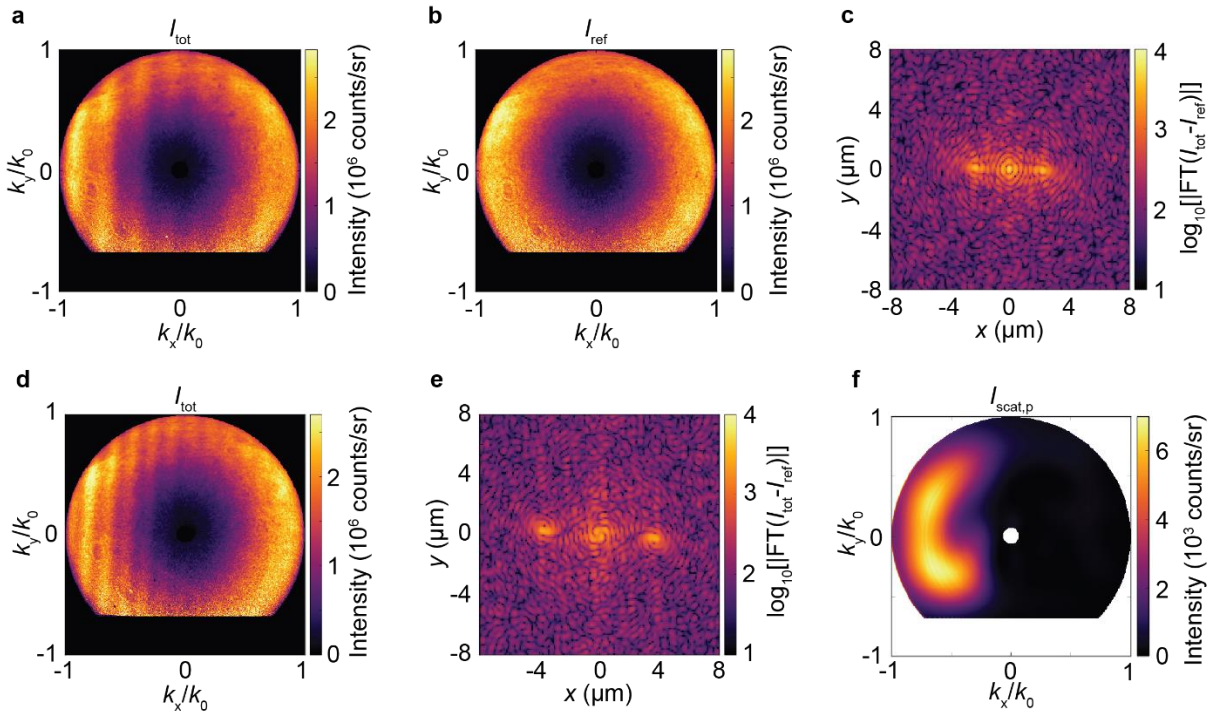

Figure S4. Interference fringes for surface plasmon polariton scattering by nanocube. Experimental results for electron beam placed (a-c): L_e=2.29 μm, (d-f): L_e=3.85 μm to the right of a 75-nm Ag nanocube. (a) Angle-resolved cathodoluminescence radiation pattern filtered with a band pass color filter (λ=600±20 nm) . (b) Reference measurement on same stack in absence of nanoscatterer. **(c)** 2D fast Fourier transform of the difference in intensity from Figs. S4a-b.

References

(1) Yang, J.; Hugonin, J. P.; Lalanne, P. Near-to-Far Field Transformations for Radiative and Guided Waves. *ACS Photonics* **2016**, *3* (3), 395–402. https://doi.org/10.1021/acsphotonics.5b00559.

(2) Röhrich, R.; Hoekmeijer, C.; Osorio, C. I.; Koenderink, A. F. Quantifying Single Plasmonic Nanostructure Far-Fields with Interferometric and Polarimetric K-Space Microscopy. *Light Sci. Appl.* **2018**, *7* (65), 1–12. https://doi.org/10.1038/s41377-018-0059-0.